Volume 55
Number 19
19 May 2026
Pages 7417-7740

Dalton Transactions

An international journal of inorganic chemistry

rsc.li/dalton

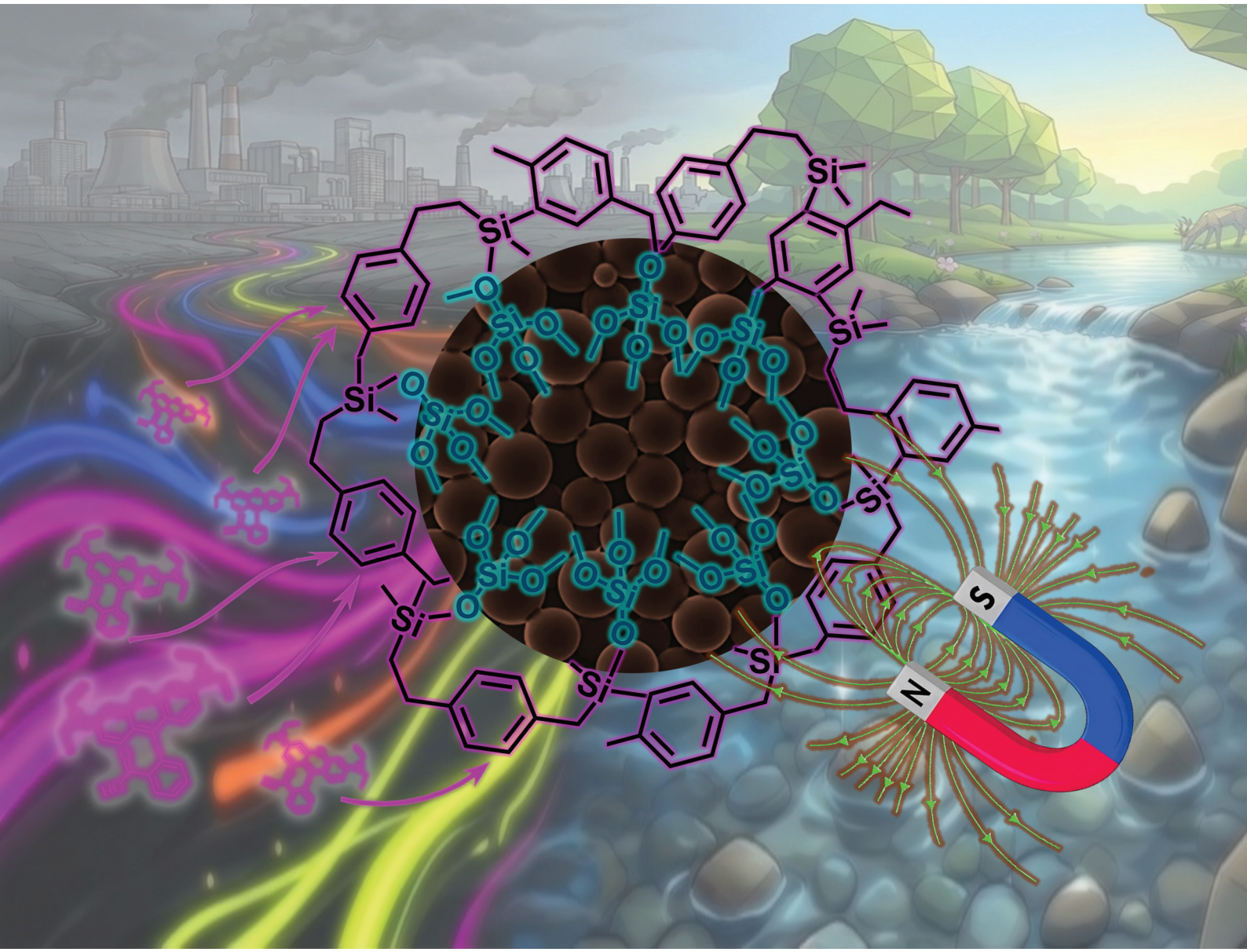

ISSN 1477-9226

ROYAL SOCIETY OF CHEMISTRY

PAPER

Sawssen Slimani, Chiara Bisio *et al.*

Magnetically recoverable swellable magnetite/SOMS hybrid nanocomposites for rapid adsorption of organic dyes from water

Dalton Transactions

ROYAL SOCIETY OF CHEMISTRY

PAPER

View Article Online
View Journal | View Issue

Cite this: *Dalton Trans.*, 2026, **55**, 7502

Magnetically recoverable swellable magnetite/SOMS hybrid nanocomposites for rapid adsorption of organic dyes from water

Lorenzo Maccarino, [a,e] Ibtissame Sidane,[b] Gianni Barucca, [c] Sawssen Slimani, *[b,d] Leonardo Marchese, [a,e] Davide Peddis [b,d] and Chiara Bisio *[a,e,f]

Received 19th January 2026,
Accepted 3rd March 2026

DOI: 10.1039/d6dt00137h

rsc.li/dalton

Hybrid magnetic adsorbents based on magnetite nanoparticles and Swellable Organically Modified Silica (Mag-SOMS) are reported for the first time to address the limited recoverability of powdered adsorbents from aqueous media. The materials are synthesised by combining magnetite nanoparticles obtained *via* different co-precipitation routes (MagA and MagB) with a SOMS matrix prepared through a sol–gel process. Structural, spectroscopic, textural, and magnetic characterisation confirms that the magnetite phase preserves its crystalline structure and magnetic properties after integration into the SOMS framework, though the hybrid materials exhibit different morphologies depending on the synthesis conditions. Both MagA-SOMS and MagB-SOMS systems remove more than 99% (1.91 mg g^{-1} adsorbed) of Rhodamine B from water within 10 minutes. The materials can be easily recovered by magnetic separation and being regenerable, can be reused for several adsorption cycles without losing their performances, highlighting their potential for water treatment applications.

Introduction

Rising levels of harmful substances due to human overconsumption are increasingly endangering natural habitats, especially water bodies. Consequently, there is an urgent need for effective mitigation strategies to minimize environmental impact. The removal of toxic pollutants from the environment remains a complex challenge, requiring a combination of physical, chemical, and biological remediation techniques.[1]

In this respect, the treatment of contaminated water is imperative before discharge. While conventional techniques like filtration, reverse osmosis, and ozonation effectively remove organic pollutants, they are often hindered by high energy consumption and the risk of generating secondary pollutants during treatment.[2]

Among the different techniques available for water treatment, adsorption is considered an effective and cost-effective method for removing organic and heavy metals contaminants.[3]

According to the recent literature, nanoparticles—particularly magnetic ones—have gained significant attention as promising candidates for wastewater remediation due to their high efficiency and ease of recovery.[4,5]

The persistent interest in room-temperature superparamagnetic spinel iron oxide nanoparticles (Fe_3O_4, γ-Fe_2O_3) stems from the possibility of precisely tailoring their magnetic response through a fine tuning of particle size, morphology, composition, and interparticle interactions. This high degree of tunability enables the rational design of functional nanostructured systems with properties optimized for specific applications, while preserving the intrinsic chemical stability and biocompatibility of magnetite.[6–8] This capability arises from significant advancements in both synthetic and diagnostic methodologies, coupled with their expanding range of applications, including biomedicine,[9] ferrofluid technology,[10] catalysis,[11,12] sensing[13] and adsorption of pollutants.[14]

In view of their significant scientific and technological relevance, a plethora of physical and chemical approaches for the synthesis of magnetite nanoparticles (MNPs) have been developed.[15,16] Among the physical methods, ball-milling

[a]*Department of Science and Technological Innovation, University of Piemonte Orientale, Viale Teresa Michel 11, Alessandria, 15121, Italy.*
E-mail: chiara.bisio@uniupo.it
[b]*Department of Chemistry and Industrial Chemistry & Genova, INSTM RU, nM2-Lab, University of Genova, Via Dodecaneso 31, Genova, 16146, Italy.*
E-mail: sawssen.slimani@unige.it
[c]*Department of Science and Engineering of Matter, Environment and Urban Planning, University Politecnica delle Marche, Via Brecce Bianche 12, 60131 Ancona, Italy*
[d]*Institute of Structure of Matter, National Research Council, nM2-Lab, Via Salaria km 29.300, Monterotondo Scalo, Roma, 00015, Italy*
[e]*Centro di Ricerca e Sviluppo per il Risanamento e la Protezione Ambientale (Centro RiSPA), Joint-Lab DISIT/Syensqo, Viale Teresa Michel 11, Alessandria, 15121, Italy*
[f]*CNR-SCITEC Institute of Chemical Science and Technology "Giulio Natta", Via G. Venezian 21, Milano, 20133, Italy*

(which encompasses both low- and high-energy variants under dry or wet conditions) stands out as a prominent technique documented in the literature.[17] Although chemical synthesis comprises various techniques, such as, thermal decomposition of metalorganic precursor, sol–gel[18] and hydrothermal[19] methods, co-precipitation is the most widely used approaches due to its simplicity and efficiency.[20] It generally involves mixing aqueous Fe(II) and Fe(III) salts with a base solution to precipitate the nanoparticles.

MNPs have been identified as a viable solution for the separation of nanosorbents after the removal of pollutants, due to their ease of magnetic recovery.[19,21] However, the utilisation of bare MNPs is frequently constrained by their propensity to agglomerate (due to elevated surface energy) and to oxidise, thus leading to the reduction of their magnetic properties.[16,22] To overcome these limitations, surface functionalization is employed. The process involves the coating of the MNPs with a protective organic or inorganic shell, which prevents aggregation and oxidation *via* electrostatic or steric repulsion. In addition, the shell can be further functionalized.[16,23] A variety of materials are employed in the synthesis of these hybrid coatings, including small organic anions (particularly citric acid[23]) and polymers,[24] as well as oxidic matrices such as zirconia,[25] titania,[26] and silica.[27]

Silica is probably the best described inorganic coating material[6] for its biocompatibility and relatively easy synthesis.[28] Silica coatings provide a surface negative charge to hybrid materials, which prevents MNPs aggregation and improves their chemical stability.[23] A silica coating is typically achieved by both Stöber and microemulsion processes.[6] The former method is the most used and involves the nucleation and growth of MNPs within a preformed silica network created from a solution of metal salts, water, ethanol, tetraethyl orthosilicate (TEOS), and ammonia.[22] By controlling the concentration of TEOS, NH_3 and water, the thickness of the silica shell can be tuned.[29] This silica shell provides a surface rich in silanol groups, which can be readily exploited for post-synthetic functionalization, thereby conferring a high degree of chemical versatility to the material.[30,31] Such functionalization can enhance key properties, including hydrophilicity/hydrophobicity, chemical stability, and specific binding affinity, which are relevant for environmental applications. However, organic functionalization, leading to hybrid silicas, is commonly achieved through two main approaches: grafting, in which organic moieties are attached after silica formation, and co-condensation, where the organic functionalities are incorporated during the synthesis process.[1]

An interesting hybrid organic–inorganic material, which has demonstrated significant potential in adsorbing various classes of pollutants from both gaseous and aqueous phases, is Swellable Organically Modified Silica (SOMS). SOMS are synthesized *via* a sol–gel process utilizing specific bis-silane monomers characterized by an internal aromatic ring. After a necessary derivatization step, the resulting material possesses the peculiar ability to swell when in contact with organic species. This property gives to the SOMS additional surface area and porosity, significantly enhancing the adsorption of organic species.[32–34]

Unfortunately, when in nanometric form, powder adsorbents are not easy to recover after their utilization, but as already pointed out, magnetite can be used for overcoming this issue. In this context, to the best of our knowledge, we present for the first time novel hybrid nanocomposite made of magnetite and SOMS, named Mag-SOMS. The synthesis of these materials and their physico–chemical characterization is here presented, along with the adsorption performance towards Rhodamine B (RhB), which has been used as a model organic dye pollutant. Finally, the recyclability of the material following the adsorption process is also described.

Experimental section

Synthesis of Mag-SOMS samples

Two different co-precipitation routes were used to prepare magnetite nanoparticles and the corresponding SOMS-based hybrid nanocomposites. The first sample, hereafter named MagA, was synthesized according to the following procedure.[35] 6.21 mmol of $FeCl_3{\cdot}6H_2O$ (>99%, Sigma-Aldrich, Schnelldorf, Germany) and 3.15 mmol of $FeCl_2{\cdot}4H_2O$ (>99%, Sigma-Aldrich, Schnelldorf, Germany) were dissolved in 100 mL of 0.01 M HCl solution (37%, Carlo Erba, Paris, France) and stirred for 1 h at 60 °C. Subsequently, 20 mL of 30% ammonium hydroxide (ACS grade, Carlo Erba, Paris, France) was added, and the reaction mixture was maintained under stirring for an additional hour. The resulting precipitate was then collected, washed 3 times with distilled water using magnetic separation, and finally dispersed in distilled water (14.2 mg mL^{-1}), with the addition of a small amount of ammonium hydroxide to adjust the pH to basic conditions.

A second sample of MNPs (named MagB) was obtained through the alkaline reverse co-precipitation method described in literature.[36,37] Briefly, 43 mL of $FeCl_3$ (97%, Merck, Darmstadt, Germany) 0.1 M aqueous solution and 25 mL of $FeSO_4$ (99.5%, Merck, Darmstadt, Germany) 0.1 M aqueous solution was mixed and then added dropwise of 25 mL of a NaOH (99%, Merck, Darmstadt, Germany) 1 M aqueous solution. After the addition of the base, the solution has been left to react for 30 minutes at RT and at 300 rpm magnetic stirring. Subsequently, the solid has been rinsed with water 2 times and with ethanol 1 time and dried.

Mag-SOMS samples were synthesized using the two MNPs types (MagA and MagB) and different MNPs : BTEB molar ratio (calculated assuming MNPs molar mass is the one of Fe_3O_4). The synthesis procedure of SOMS was adapted from previous works,[32,34] and requires the addition of the monomer bis(trimethoxysilylethyl)benzene (BTEB, 97%, Gelest Inc., Morrisville, PA, USA), tetrahydrofuran (THF, HPLC grade, Fisher Scientific, Loughborough, UK) as organic solvent, and Tetrabutylammonium fluoride (TBAF, 1.0 M in methanol, Acros Organics, Geel, Belgium) as catalyst.

The synthesis of the first composite material, named MagA-SOMS, was carried out using 2.5 mL of MagA dispersion (corresponding to 35.5 mg of magnetite) to which 514 μL of BTEB, 2.490 mL of THF and 3.5 μL of TBAF were added and left to react for 24 hours at RT and 300 rpm stirring rate. The molar ratio MagA : BTEB is 1 : 9.4.

For the synthesis of the second sample, hereafter named MagB-SOMS, 300 mg of MagB were dispersed in 10.5 mL of THF and then 2.346 mL of BTEB, 656 μL of H_2O and 15 μL of TBAF were added. The molar ratio MagB : BTEB is 1 : 5.2. The reagents were left to react for 24 hours at RT and 300 rpm stirring rate.

After the synthesis, both MagA-SOMS and MagB-SOMS were rinsed with acetonitrile (ACN, HPLC grade, Fisher Scientific, Loughborough, UK) three times. Then, both the materials were subject to derivatization with a 5% v/v solution of hexamethyldisilazane (HMDS, >99%, Merck, Darmstadt, Germany) in ACN for 3 days at RT and 300 rpm stirring rate. Finally, the materials were washed with ACN three times and dried at 60 °C for 24 hours.

The synthesis processes for MagA-SOMS and MagB-SOMS is represented in Fig. 1.

Characterization techniques

The X-Ray Diffraction (XRD) patterns of the different materials were obtained with a Bruker D8 advance diffractometer (Karlsruhe, Germany) with Bragg–Brentano geometry, with Cu anode (λ = 1.5418 Å) equipped with a Ni filter and operating at 40 kV and 40 mA. The 2θ explored was of 5–70°, with 2θ steps of 0.02°, 0.1 s per step, and automatic synchronization of the anti-scatter knife.

Transmission electron microscopy (TEM) analysis was carried out using a CM200 microscope (Philips, Amsterdam, The Netherlands.) operating at 200 kV and equipped with a LaB_6 filament. The samples in the form of powder were dispersed in ethanol and ultrasonicated for a minute. A drop of suspension was deposited on a commercial TEM grid covered with a holey-carbon thin film and maintained in air until complete evaporation of the solvent.

Scanning electron microscopy (SEM) micrographs were acquired using a GeminiSEM 360 scanning electron microscope (Zeiss, Oberkochen, Germany) equipped with a Schottky field emission source. In high vacuum mode, the instrument achieves a vacuum of 10^{-6} mbar in the sample chamber and 10^{-10} mbar in the electron column. Prior to the analysis, to prevent insulating particles from becoming electronically charged under the electron beam, a conductive platinum coating (a few nm) was deposited on the samples by chemical vapor deposition (CVD) using a DSCT-F sputter coater (VacCoat, London, UK). Thickness control is achieved using a quartz microbalance crystal (FTM – Film Thickness Monitor). The gas used for plasma generation is argon. The vacuum in the chamber before and after argon is introduced is 4×10^{-5} mbar and 4×10^{-3} mbar, respectively. The elemental maps (EDX) were acquired with the UltimMax 65 detector (Oxford Instruments, Abingdon-on-Thames, United Kingdom), which has an active sensor area of 65 mm^2 (SDD – Silicon Drift Detector) and an energy resolution of ~125 eV at Mn Kα (5.9 keV). The X-ray detector is cooled by a Peltier refrigeration system.

Nitrogen sorption measurements were performed at 77 K in the pressure range between 0.01 and 1 of relative pressure (P/P_0) using a Autosorb-iQ (Quantachrome Instruments). Before the adsorption phase, the samples were outgassed and thermally treated at 150 °C for 5 h. The specific surface area of the samples was determined by the Brunauer–Emmett–Teller (BET) multipoint method, while the pore size distributions was obtained by applying the NLDFT method on the adsorption branch of the isotherms (silicas and cylinder pore model).

Micro-Fourier Transformed-Infrared (μ-FT-IR) measurements were performed on materials deposited on silver metal membrane filters (Sterlitech; pore size 0.8 μm, Ø = 13 mm) using a Nicolet iN10 MX Infrared Imaging Microscope (Thermo Scientific, Waltham, MA, USA) controlled by OMNIC Picta software (Thermo Scientific, Waltham, MA, USA) in reflectance mode. Focusing was performed in spectral preview mode, 256 scans (range 4000–675 cm^{-1}) were acquired for each spectrum with 4 cm^{-1} resolution, and Beer–Norton apodization applied. The obtained spectra were subjected to baseline and smoothing corrections using the respective tools given by the OPUS (Version 5.5) software and then range scaled between 0 and 1.

DC magnetization measurements were performed using a Physical Property Measurement System (PPMS, Quantum Design) magnetometer (H_{max} = 7 T; T = 5–400 K). The powdered sample was fixed in a polycarbonate capsule using epoxy resin to prevent any movement during the measurements. All magnetic data were normalized to the actual mass of the magnetic phase. The saturation magnetization (M_S) was deter-

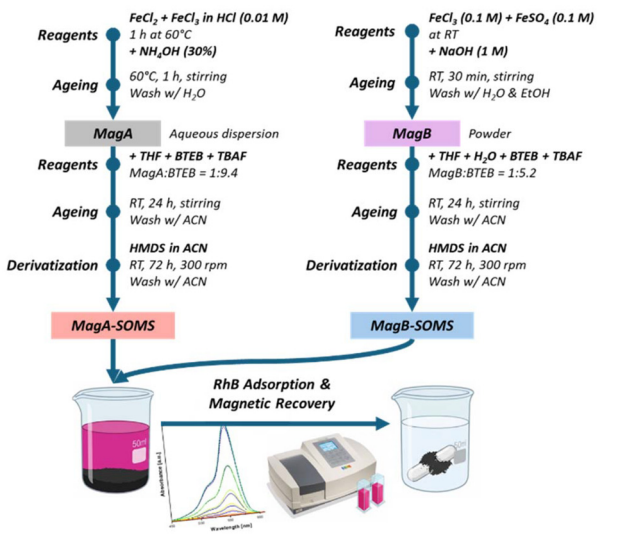

Fig. 1 Schematic representation of the steps for the synthesis of MagA-SOMS and MagB-SOMS starting from the synthesis by co-precipitation of the two magnetite samples (MagA and MagB).

mined by fitting the high-field region of the $M(H)$ curves using the following expression:[38]

$$M = M_S\left(1 - \frac{A}{H} - \frac{B}{H^2}\right)$$

Rhodamine B adsorption test

The materials were evaluated for their ability to adsorb Rhodamine B (RhB, ≥95%, Merck, Darmstadt, Germany) dye from an aqueous solution. The adsorption kinetics were studied under the following experimental conditions: a 10 mL aliquot of a 20 μM RhB solution was combined with 50 mg of the adsorbent. Only for MagA-SOMS and MagB-SOMS, a pre-swelling with 100 μL of ethanol was done before contact with RhB solution.

The RhB adsorption was investigated by UV-vis spectroscopy using a Lambda 900 UV-visible spectrometer (PerkinElmer, Waltham, MA, USA). An aqueous solution aliquot was withdrawn at specific time intervals to monitor the RhB concentration: every 2.5 minutes for the first 10 minutes, then every 5 minutes until 45 minutes, with a final measurement after 60 minutes. To evaluate the RhB percentage in solution ($C_{\%}$) the following equation was used:

$$C_{\%} = \frac{A(t)}{A_0} \times 100$$

where $A(t)$ is the absorbance at maximum wavelength (554 nm) of RhB after a certain time, t, and A_0 is the absorbance at 554 nm of the initial RhB solution.

Consequently, the RhB percentage adsorbed ($C_{\%,ads}$) can be calculated as:

$$C_{\%,ads} = 100 - C_{\%}$$

To calculate the quantity of RhB adsorbed as a function of time (q_t in mg g^{-1}), the following equation has been used:

$$q_t = \frac{(C_0 - C_t)}{m} \times V \times MM_{RhB} \times 1000$$

where C_0 is the initial concentration of RhB (20 μM), C_t is the molar concentration at specific time, obtained by dividing $A(t)$ over the molar extinction coefficient of RhB at 554 nm (104 900 L mol^{-1} cm^{-1})[32] and considering an optical path of 1 cm, V is the volume of the RhB solution used (0.010 L), m is the mass of the adsorbent used (0.050 g) and MM_{RhB} is the molar mass of RhB (479.02 g mol^{-1}).

To evaluate the reusability of MagB-SOMS, the composite was subjected to six adsorption–desorption cycles. Following RhB adsorption (20 min contact time), the material was recovered and placed in 10 mL of ethanol. Desorption was performed by sonicating the mixture for 10 minutes at room temperature. The resulting powder was then recovered and dried for 2 hours at 80 °C before undergoing the subsequent adsorption procedure as previously described.

The quantity of RhB desorbed (q_{des}) can be calculated in the following manner:

$$q_{des} = \frac{C_{des}}{m} \times V_{EtOH} \times MM_{RhB} \times 1000$$

where C_{des} is the desorbed concentration of RhB, obtained by dividing the absorbance of the solution over the molar extinction coefficient of RhB at 545 nm (91 300 L mol^{-1} cm^{-1})[32] and considering an optical path of 1 cm, V_{EtOH} is the volume of the ethanol used (0.010 L), m is the mass of the adsorbent (0.050 g) and MM_{RhB} is the molar mass of RhB (479.02 g mol^{-1}).

Moreover, the quantity of RhB retained by the material ($q_{ret,i}$) after every adsorption–desorption cycle, can be calculated as follows:

$$q_{ret_i} = q_{ret_{i-1}} + q_{ads_i} - q_{des_i}$$

where $q_{ret,i-1}$ is the quantity retained by the material from the previous cycle, $q_{ads,i}$ and $q_{des,i}$ are the quantity adsorbed after 20 minutes of contact and desorbed, respectively, at the i-th cycle.

Results and discussion

XRD patterns (Fig. 2) show the presence of a cubic spinel structure (JCPDS card no. 19-0629) in all the samples. Residual goethite phase was found in MagB sample, as testified by the presence of reflections at 21.3°, 33.3°, 47.2° and 59.1° 2θ.[39] Goethite formation is primarily favoured under mildly acidic to near-neutral conditions (pH ≈ 5–7) and at relatively low temperatures (below ~60 °C); under these conditions, the presence of goethite impurities can additionally be attributed to partial oxidation of Fe^{2+} species,[40] likely promoted by the synthesis being carried out in a non-inert atmosphere.[23] No significant differences are visible in the XRD patterns of MagB before and after the addition of SOMS shell. For MagA-SOMS samples, a low intensity and broad band in the 2θ region from 13° and 27°, due to amorphous silica, can be observed.[37]

The samples' morphology was investigated using transmission electron microscopy (TEM). High-resolution (HR) TEM of the bare particles (Fig. S1) reveals that MagA particles exhibit a quasi-spherical shape, whereas MagB particles are generally faceted, as a consequence of the different synthesis procedure.[35] Fig. 3 shows bright-field and HR-TEM images of the functionalized particles, MagA-SOMS (frames a, c) and MagB-SOMS (frames b, d). The analysis confirms the presence of magnetic nanoparticles dispersed within the SOMS matrix

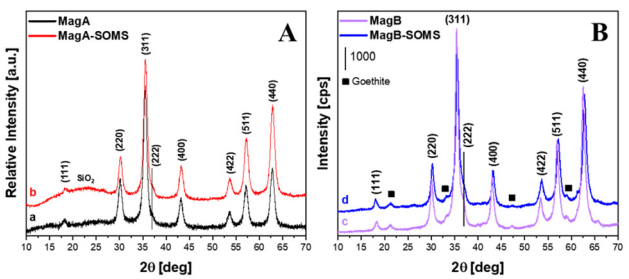

Fig. 2 XRD pattern of (A) MagA (a – black) and MagA-SOMS (b – red) and (B) of MagB (c – violet) and MagB-SOMS (d – blue).

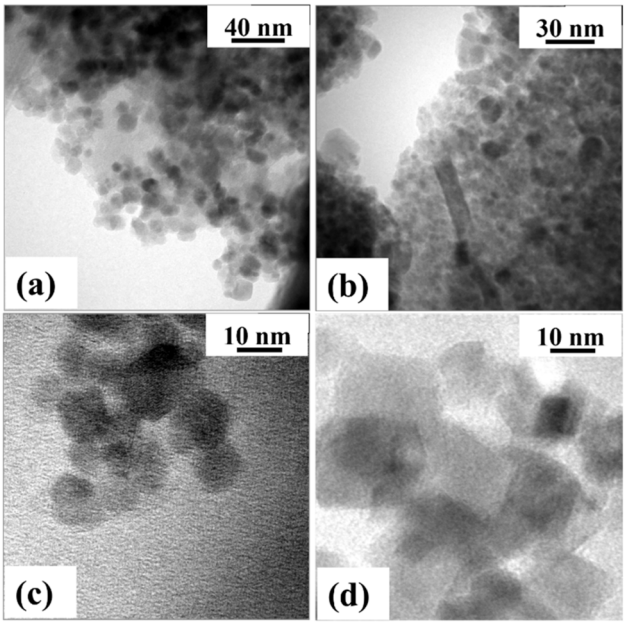

Fig. 3 Bright-field TEM images showing the dispersion of magnetic nanoparticles within the amorphous SOMS matrix of (a) MagA-SOMS and (b) MagB-SOMS. HR-TEM images showing (c) quasi-spherical MagA and (d) faceted MagB nanoparticles embedded within the SOMS matrix.

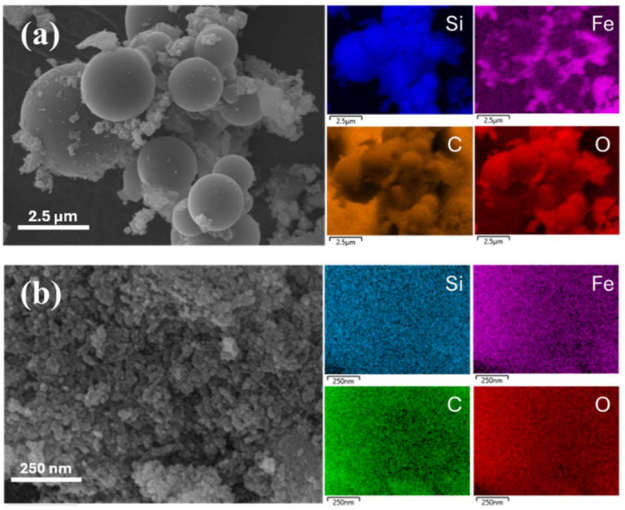

Fig. 4 SEM micrographs (left) and EDX elemental mapping (right, elements are reported on the figure) of (a) MagA-SOMS, and (b) MagB-SOMS samples.

in both systems. Despite the different physical states of the starting magnetic particles (MagB powder and MagA dispersion), TEM observations reveal that the nanoparticles tend to form aggregates in the SOMS composites, and no clear or systematic differences in aggregation behaviour can be reliably discerned when comparing the two samples.

Scanning electron microscopy (SEM) was employed to investigate the morphology and phase organization of the hybrid materials at the micrometre and sub-micrometre scale. MagA-SOMS (Fig. 4a and Fig. S2) possesses larger particles with spherical morphology, with diameters in the order of micrometres (from 1 to 4 μm), principally made of silica SOMS, and smaller ones made of magnetite. The elemental content determined by EDX was found to be 69 wt% C, 19 wt% O, 9 wt% Si, and 3 wt% Fe. A different morphology has been noted for the MagB-SOMS sample (Fig. 4b). This latter material shows a morphology similar to bare SOMS,[33] where aggregates of nanoparticles having irregular shape and different dimensions (of the order of less than 100 nm) are present. EDX analysis revealed the elemental composition (in wt%) to be 27% C, 18% O, 2% Si, and 53% Fe. The difference in morphology and elemental composition, in particular Si and Fe, between MagA-SOMS and MagB-SOMS samples can be explained by considering the nature of the starting solution of the MNPs used for the creation of the hybrid material. In the case of MagA-SOMS, the MNPs were dispersed in an aqueous solution at pH ~11.7, and the SOMS shell was synthesized by directly adding the required reactants to the basic dispersion. While for the MagB-SOMS, MagB nanopowders were directly used: in this case the pH of the synthetic solution corresponds to that of SOMS reactants, starting at 7.2 and rapidly increasing to values above 12.5 after TBAF addition. In the former case, a phase separation likely occurs between the aqueous MagA dispersion and BTEB/THF phase, resulting in a microemulsion-like synthesis, leading to the formation of spherical micrometric MagA-SOMS.[41–43]

The textural properties of MagA-SOMS and MagB-SOMS were analysed by N_2 physisorption at 77 K, thus allowing the assessment of specific surface area and porosity of the two hybrid systems in powder form. The adsorption–desorption isotherms and pore size distribution of the composite materials are reported in Fig. S3a and b. The specific surface area (SSA) was determined by applying the Brunauer–Emmett–Teller (BET) method, which provided for MagA-SOMS and MagB-SOMS ~85 and ~90 $m^2\ g^{-1}$, respectively. Both samples showed a type IV isotherm with an H4 type hysteresis loop. For MagA-SOMS, the incomplete closure of the adsorption–desorption loop, persisting down to low relative pressures ($P/P_0 \approx 0.05$), indicates a swelling behaviour of the material, in agreement with previous observations reported for pure SOMS.[32,44] Analysis of the pore size distribution can be found in SI.

The samples were further characterized by FTIR microscopy in reflectance mode (Fig. S4) to probe the chemical structure of the hybrid materials. This technique allows the identification of characteristic vibrational modes of the silica framework and organic moieties, thus assessing the presence and integrity of functional groups and possible interactions between the SOMS matrix and the magnetic nanoparticle. In both MagA-SOMS and MagB-SOMS, the most evident deviation from the SOMS reference spectrum occurs in the O–H stretching region (3800–3100 cm^{-1}), while the rest of the spectral features remain essentially unchanged, indicating that the SOMS framework is preserved. The two overlapping bands found between 3800–3100 cm^{-1} change their intensity in the two

hybrid materials and the one centred at around 3450 cm^{-1} is much broader than in the spectrum of pure SOMS. This is probably due to the presence not only of Si–OH groups, deriving from SOMS shell, but also from Fe–OH groups of MNPs.[39]

Magnetic properties

To investigate the influence of the functionalization with SOMS on the magnetic properties, the field and temperature-dependent magnetization were measured for both synthesized bare iron oxide nanoparticles (MagA and MagB) and their hybrid nanocomposites counterparts (MagA-SOMS and MagB-SOMS). Magnetization curves recorded at 5 K and 300 K (Fig. 5a and b) show that the SOMS encapsulation of MNPs does not significantly affect their magnetic properties. Both bare MNPs and their hybrid nanocomposites exhibit similar saturation magnetization (M_s) and coercive field (H_c) values (Table 1), within the experimental error, clearly indicating that SOMS presence does not affect the magnetic features of the MNPs.

This result deserves attention, as the presence of a molecular coating and its interaction with the nanoparticle surface may induce significant variations in the magnetic properties.[45,46] At 300 K, the $M(H)$ curves (insets of Fig. 5a and b) display superparamagnetic behaviour for all samples, characterized by zero remanent magnetization ($M_r = 0$) and zero coercive field ($H_c = 0$). The observed small difference in saturation magnetization between the MagA and MagB samples is attributed to the presence of an additional phase in MagB (antiferromagnetic Goethite), as confirmed by XRD analysis, that leads to the reduction the M_s.

The thermal dependence of the magnetization measured using zero-field-cooled (ZFC) and field-cooled (FC) protocols in a DC field of 2.5 mT, over the temperature range 5–300 K, is shown in Fig. 6a and b. In typical ZFC measurements, the samples were first cooled from 300 to 5 K in zero magnetic field, then a field of 2.5 mT was applied, and the magnetization was recorded during warming from 5 to 300 K. The same field was maintained while cooling the samples back to 5 K, and the FC magnetization was measured during the warming process.

The obtained ZFC/FC curves display a behaviour typical of ensembles of single-domain MNPs with a distribution of blocking temperatures. For both MagA and MagA-SOMS samples, the ZFC magnetization curve exhibits a broad maximum, which is considered proportional to the mean blocking temperature, $T_{max} = \beta T_b$, where β depends on the size distribution.[47] The blocking temperature, T_b, is defined as the temperature at which the magnetic relaxation time of the nanoparticles equals the characteristic measuring time of the experimental technique.[48] In real nanoparticle systems, where a finite particle size distribution is always present, a distribution of blocking temperatures is therefore expected. Accordingly, T_b is often determined when approximately 50% of the nanoparticles are in a superparamagnetic state.[49] The distribution of blocking temperatures can be derived from the distribution of anisotropy energy barriers (ΔE_a) by evaluating the temperature at which 50% of the particles can overcome their anisotropy barriers within the experimental time window (Fig. S5). In addition, both samples show an irreversibility between the FC and ZFC curves persisting up to relatively high temperatures (T_{irr}), which is associated with the blocking of the largest particles. All FC magnetization curves show a temperature-independent behaviour at low temperatures, suggesting the presence of interparticle interactions among the particles.[50] These interactions can reasonably be ascribed to particle aggregation, in agreement with TEM analysis,

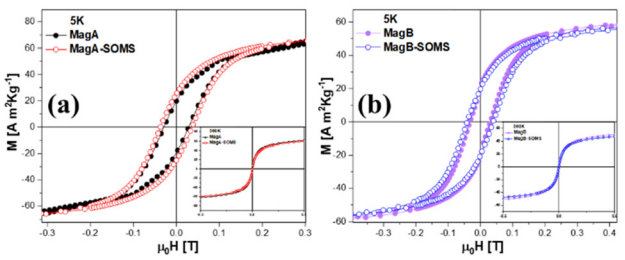

Fig. 5 Magnetization as a function of the applied magnetic field at 5 K for (a) MagA and (b) MagB MNPs, before and after SOMS encapsulation. Insets: magnetization curves measured at 300 K.

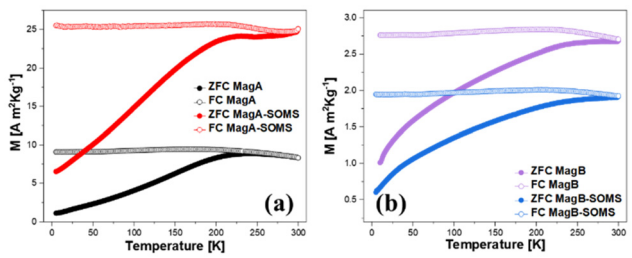

Fig. 6 Thermal dependence of magnetization measured according to the ZFC/FC protocols at 2.5 mT. ZFC (full symbols) and FC (empty symbols) for (a) bare MNPs MagA, and functionalized particles MagA-SOMS; (b) bare MNPs MagB and functionalized MagB-SOMS.

Table 1 Saturation magnetization (M_s) at 300 K and 5 K, coercive field ($\mu_0 H_c$) and reduced remanent magnetization (M_r/M_s) at 5 K, blocking temperature (T_b) and irreversibility temperature (T_{irr}) determined from the ZFC/FC curves. Uncertainties on the last digit are given in parentheses.

Sample	$M_{s\ 300K}$ [A m^2 kg^{-1}]	$M_{s\ 5K}$ [A m^2 kg^{-1}]	$\mu_0 H_c$ [mT]	M_r/M_s	T_b [K]	T_{irr} [K]
MagA	72 (1)	83 (1)	30 (1)	0.24	131 (1)	242 (3)
MagA-SOMS	70 (3)	80 (1)	36 (1)	0.31	112 (2)	276 (1)
MagB	67 (1)	70 (1)	29 (2)	0.32	—	—
MagB-SOMS	55 (2)	67 (1)	39 (2)	0.31	—	—

which decreases the average interparticle spacing and enhances dipolar interactions, thereby deviating from an ideal non-interacting superparamagnetic regime. Comparison of the T_b and T_{irr} values (Table 1) indicates that the MagA-SOMS sample exhibits lower T_b than MagA, which corresponds to the reduction of particle aggregation. In contrast, MagB and MagB-SOMS samples exhibit very similar thermal magnetic behaviour. In both cases, no clear maximum is observed in the ZFC curves, and the FC curves remain largely temperature independent. This indicates that both systems are highly interacting, with a characteristic blocking temperature exceeding the room temperature. This observed difference with respect to the MagA-based samples is consistent with the higher structural and magnetic heterogeneity of MagB. Moreover, while MagA-SOMS was prepared starting from a well-dispersed particle suspension, MagB-SOMS was obtained directly from MagB powder, resulting in a highly interacting system already at the initial stage.

Rhodamine B adsorption test

The adoption of two distinct co-precipitation routes for the synthesis of iron oxide magnetic nanoparticles, combined with the preparation of two corresponding SOMS-based hybrid nanocomposites – ranging from a microemulsion-like process in the case of MagA-SOMS to a more conventional sol–gel assembly for MagB-SOMS – was designed to evaluate if the nanoparticle structure and morphology influence the adsorption performance of the Mag-SOMS materials. Importantly, this strategy enabled the decoupling of adsorption behaviour from both the magnetic nanoparticle synthesis and the specific nanocomposite morphology.

From the RhB adsorption kinetics (Fig. 7), it can be observed that both MagA-SOMS and MagB-SOMS effectively remove more than 99% (1.91 mg g^{-1}) of RhB in less than 10 minutes. Moreover, the adsorption rate is comparable for the two materials, confirming that the incorporation of goethite does not hinder either the magnetic recovery or the adsorption efficiency. From a mechanistic perspective, and as a potentially useful consideration for the design of new materials, it is worth noting that goethite (α-FeOOH) is known to interact strongly with adsorbates due to the presence of surface hydroxyl groups (≡Fe–OH), which act as active sites for binding organic molecules through hydrogen bonding. These hydroxyl groups are widely recognized as key contributors to the adsorption of both organic and inorganic species on goethite and other iron oxyhydroxides. Therefore, the presence of goethite may provide additional surface active sites, potentially contributing to the maintained high adsorption performance observed for MagB-SOMS.[51]

This behaviour is identical to the one found for bare SOMS.[32] The bare magnetite nanoparticles (MagB), on the contrary, do not adsorb effectively RhB, the concentration of which is reduced, in fact, only around 10% (0.36 mg g^{-1} adsorbed) in the first hour of contact. The difference between hybrid materials and bare magnetite demonstrates that the SOMS shell is responsible of the enhanced adsorption performances. Indeed, by comparing the behaviour of MagA-SOMS and MagB-SOMS, it is clear that the adsorption efficiency toward Rhodamine B is primarily governed by the SOMS component and remains largely independent by the preparation route of both the magnetic nanoparticles and the hybrid nanocomposite. This confirms the robustness and versatility of the Mag-SOMS synthetic strategy.

Given that the SOMS component constitutes the active phase for adsorption, the governing mechanisms are expected to parallel those established for pure SOMS that have already been explained in our previous article.[32] These interactions include: (i) electrostatic attraction between the negatively charged SOMS surface and the cationic or zwitterionic forms of RhB dye in aqueous solution;[32] (ii) non-covalent apolar π–π stacking between SOMS framework and RhB aromatic rings;[33,52,53] (iii) swelling-induced porosity, where the pre-swelling step increases the accessible pore volume available for adsorption thus maximizing pore accessibility.[54]

The possibility to recover the magnetic hybrid nanocomposites after adsorption was tested using a commercial stirring bar immersed in the aqueous solution. In Fig. 8 the complete workflow is presented as follows: (i) initial contact between the RhB aqueous solution (purple coloured) and the hybrid material on the bottom (dark brown powder); (ii) mixing of the two components; (iii) magnetic decantation of the powder from the aqueous solution (which is visibly unco-

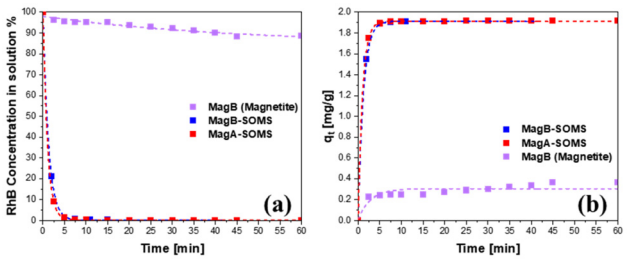

Fig. 7 Adsorption kinetics of RhB by MagA-SOMS (red) and MagB-SOMS (blue) compared to MagB (bare magnetite, in violet) expressed as (a) RhB residual % concentration in solution, $C_{\%}$, and (b) quantity of RhB adsorbed in mg g^{-1} over time. Experimental conditions: 50 mg of the material put in contact with 10 mL of a RhB aqueous solution with initial concentration of 20 μM.

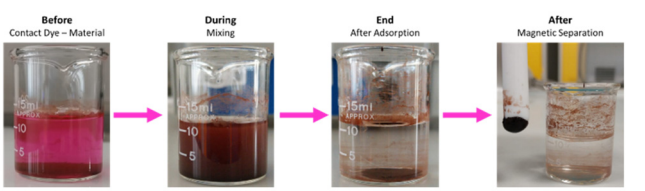

Fig. 8 Experimental images and workflow followed. From left to right: passing from the initial contact between the RhB aqueous solution and the hybrid material, to the mixing of the two components, to the magnetic decantation of the material from the aqueous solution, visibly uncoloured, to the magnetic separation and recovery of the hybrid material with a commercial magnetic stirring bar.

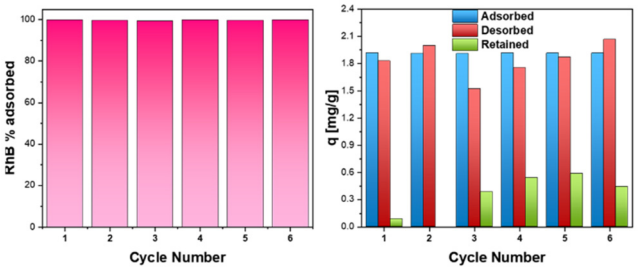

Fig. 9 (a) RhB C% adsorbed and (b) quantity of RhB adsorbed (blue bars), desorbed (red bars) and retained (green bars), in mg g^{-1}, by MagB-SOMS as a function of adsorption–desorption cycle number.

loured); (iv) separation and recovery of Mag-SOMS, after adsorption, using a commercial magnetic stirring bar. It can be clearly seen that the magnetic hybrid nanocomposite can be easily recovered from the solution.

A comparison of the adsorption capacities of the synthesized adsorbents with other materials is summarised in Table S1, which details both the adsorbed quantity of RhB and the corresponding removal percentage. It should be noted that direct comparisons of adsorption capacities can be difficult due to the wide variety of reported experimental conditions. Consequently, a representative selection of earlier studies is presented. To facilitate comprehensive evaluation, Table S1 explicitly outlines the main experimental parameters associated with each reported value. From the comparison, Mag-SOMS composites outstand for their rapidity in RhB removal (10 min) and very high percentage of dye adsorbed at relatively low initial concentrations of RhB.

In order to evaluate the practical applicability and lifespan of the composite, the regenerability and reusability of MagB-SOMS were investigated over multiple adsorption–desorption cycles. The procedure of regeneration was executed by sonication of the composite in ethanol, as described in the Experimental section. As Fig. 9 shows, the efficiency of removal and the quantities of RhB adsorbed, desorbed, and retained by the composite were monitored across six consecutive cycles (exact values in Table S2). As shown in Fig. 9, MagB-SOMS demonstrated exceptional reusability; the adsorption capacity remains stable at *ca.* 1.91 mg g^{-1} over six cycles, maintaining a removal efficiency higher than 99%. Sonication-based regeneration in ethanol proved highly effective, recovering >1.50 mg g^{-1} of the dye per cycle. Notably, the minor fraction of RhB remaining within the composite did not impair subsequent performance, a behavior mirroring previous observations for pure SOMS.[32]

Conclusions

In this work, to the best of our knowledge, hybrid magnetic adsorbents based on magnetite nanoparticles and Swellable Organically Modified Silica (Mag-SOMS) are reported for the first time. The proposed strategy effectively combines the high adsorption capability of SOMS with the magnetic responsiveness of spinel iron oxides (Fe_3O_4), overcoming the intrinsic limitations related to the difficult recovery from aqueous media of adsorbents in the form of nanopowders.

Two Mag-SOMS systems, obtained from magnetite nanoparticles synthesised *via* different co-precipitation routes and assembled through distinct sol–gel pathways, were investigated to decouple the influence of magnetic core preparation and composite formation route from the adsorption performance. Structural, morphological, textural, spectroscopic, and magnetic analyses confirm that the magnetite phase preserves its crystalline structure and magnetic behaviour after SOMS encapsulation, while the hybrid materials exhibit different morphologies and porosity features depending on the synthesis conditions.

Despite these differences, both MagA-SOMS and MagB-SOMS display outstanding adsorption efficiency toward Rhodamine B, removing more than 99% of the dye from aqueous solution within ten minutes. The kinetics and efficiency are comparable to those of bare SOMS, and the bare magnetite nanoparticles show negligible RhB uptake, demonstrating that the adsorption process is governed primarily by the SOMS component, and is largely independent by both the magnetic nanoparticle synthesis route and the composite morphology.

It is relevant underlining that the hybrid materials can be rapidly and efficiently recovered from water by simple magnetic separation, thus demonstrating the robustness, versatility, and effectiveness of Mag-SOMS as magnetically recoverable adsorbents, and this opens promising perspectives for their application in environmental remediation and wastewater treatment.

Author contributions

Lorenzo Maccarino: conceptualization, methodology, validation, formal analysis, investigation, data curation, writing – original draft, writing – review & editing, visualization. Ibtissame Sidane: conceptualization, methodology, validation, formal analysis, investigation, data curation, writing – original draft, writing – review & editing, visualization. Gianni Barucca: formal analysis, investigation, resources, writing – review & editing. Sawssen Slimani: conceptualization, methodology, validation, formal analysis, investigation, data curation, writing – original draft, writing – review & editing, visualization. Leonardo Marchese: resources, writing – review & editing, supervision, project administration, funding acquisition. Davide Peddis: conceptualization, methodology, resources, writing – original draft, writing – review & editing, supervision, project administration, funding acquisition. Chiara Bisio: conceptualization, methodology, resources, writing – review & editing, supervision, project administration, funding acquisition.

Conflicts of interest

There are no conflicts to declare.

Data availability

The supporting data has been provided as part of the supplementary information (SI). Supplementary information: Fig. S1–S4, HR-TEM, N_2 physisorption isotherms, μFT-IR spectra and Magnetic measurements. See DOI: https://doi.org/10.1039/d6dt00137h.

Acknowledgements

D. P. and S. S. acknowledge the support of the "Network 4 Energy Sustainable Transition NEST" project (code PE0000021), adopted by the "Ministero dell'Università e della Ricerca (MUR)", according to attachment E of Decree No. 1561/2022. L. M., L. M. and C. B. acknowledge the support of the "NODES Project – Nord Ovest Digitale E Sostenibile" (code ECS_36e CUP C13C22000420001). L. M., L. M. and C. B. also thank Federico Begni for BET measurements and Vanessa Miglio for SEM-EDX images.

References

1 A. Grisolia, G. Dell'Olio, A. Spadafora, M. De Santo, C. Morelli, A. Leggio and L. Pasqua, *Molecules*, 2023, **28**, 5105.
2 G. Crini, *Bioresour. Technol.*, 2006, **97**, 1061–1085.
3 Z. Ezzeddine, I. Batonneau-Gener, G. Ghssein and Y. Pouilloux, *Water*, 2025, **17**, 669.
4 J. Mo, H. Lu, J. Liu, X. Liang, W. Li and Y. Deng, *J. Water Process Eng.*, 2025, **71**, 107295.
5 A. A. Almehizia, M. K. Abosaoda, A. Kumar, V. Jain, S. Ballal, A. Singh, K. Jayabalan, S. Ray, P. Rajput and O. P. Doshi, *Sci. Rep.*, 2025, **15**, 25859.
6 R. G. Digigow, J.-F. Dechézelles, H. Dietsch, I. Geissbühler, D. Vanhecke, C. Geers, A. M. Hirt, B. Rothen-Rutishauser and A. Petri-Fink, *J. Magn. Magn. Mater.*, 2014, **362**, 72–79.
7 S. Bandyopadhyay, H. Zafar, M. S. Khan, R. Ansar, D. Peddis, S. Slimani, N. Bali, Z. Sajid, R. E. M. Qazi, F. Ur Rehman and A. A. Mian, *J. Colloid Interface Sci.*, 2025, **678**, 873–885.
8 G. Muscas, F. Congiu, G. Concas, C. Cannas, V. Mameli, N. Yaacoub, R. S. Hassan, D. Fiorani, S. Slimani and D. Peddis, *Nanoscale Res. Lett.*, 2022, **17**, 98.
9 M. Weißpflog, N. Nguyen, N. Sobania and B. Hankiewicz, *J. Phys. Chem. C*, 2024, **128**, 15598–15612.
10 C. Scherer and A. M. Figueiredo Neto, *Braz. J. Phys.*, 2005, **35**, 718–727.
11 S. Alberti, V. Caratto, D. Peddis, C. Belviso and M. Ferretti, *J. Alloys Compd.*, 2019, **797**, 820–825.
12 F. Papatola, S. Slimani, D. Peddis and A. Pellis, *Microb. Biotechnol.*, 2024, **17**, e14481.
13 F. Garkani Nejad, S. Tajik, H. Beitollahi and I. Sheikhshoaie, *Talanta*, 2021, **228**, 122075.
14 B. Elhadj-Daouadji, F. Zaoui, M. A. Zorgani, S. Abubakar, L. A. Siddig, A. S. Abdelhamid, M. Bhardwaj, M. Hachemaoui, M. Guezzoul, A. Kumar, B. Bounaceur, F. Lebsir and N. Saleh, *Fuel*, 2025, **381**, 133284.
15 C. Cannas, A. Musinu, D. Peddis and G. Piccaluga, *J. Nanopart. Res.*, 2004, **6**, 223–232.
16 S. Liu, B. Yu, S. Wang, Y. Shen and H. Cong, *Adv. Colloid Interface Sci.*, 2020, **281**, 102165.
17 G. Ennas, G. Marongiu, S. Marras and G. Piccaluga, *J. Nanopart. Res.*, 2004, **6**, 99–105.
18 I.-C. Masthoff, M. Kraken, D. Mauch, D. Menzel, J. A. Munevar, E. Baggio Saitovitch, F. J. Litterst and G. Garnweitner, *J. Mater. Sci.*, 2014, **49**, 4705–4714.
19 D. Capsoni, P. Lucini, D. M. Conti, M. Bianchi, F. Maraschi, B. De Felice, G. Bruni, M. Abdolrahimi, D. Peddis, M. Parolini, S. Pisani and M. Sturini, *Nanomaterials*, 2022, **12**, 4330.
20 S. Slimani, G. Concas, F. Congiu, G. Barucca, N. Yaacoub, A. Talone, M. Smari, E. Dhahri, D. Peddis and G. Muscas, *J. Phys. Chem. C*, 2021, **125**, 10611–10620.
21 A. Shahzad, B. Aslibeiki, S. Slimani, S. Ghosh, M. Vocciante, M. Grotti, A. Comite, D. Peddis and T. Sarkar, *Sci. Rep.*, 2024, **14**, 17674.
22 C. Cannas, A. Musinu, G. Piccaluga, D. Fiorani, D. Peddis, H. K. Rasmussen and S. Mørup, *J. Chem. Phys.*, 2006, **125**, 164714.
23 S. Laurent, D. Forge, M. Port, A. Roch, C. Robic, L. Vander Elst and R. N. Muller, *Chem. Rev.*, 2008, **108**, 2064–2110.
24 F. Sharifianjazi, M. Irani, A. Esmaeilkhanian, L. Bazli, M. S. Asl, H. W. Jang, S. Y. Kim, S. Ramakrishna, M. Shokouhimehr and R. S. Varma, *J. Mater. Sci. Eng. B*, 2021, **272**, 115358.
25 A. K. Chitoria, A. Mir and M. A. Shah, *Ceram. Int.*, 2023, **49**, 32343–32358.
26 A. Wojciechowska, A. Markowska-Szczupak and Z. Lendzion-Bieluń, *Materials*, 2022, **15**, 1863.
27 A. Lazzarini, R. Colaiezzi, M. Passacantando, F. D'Orazio, L. Arrizza, F. Ferella and M. Crucianelli, *J. Phys. Chem. Solids*, 2021, **153**, 110003.
28 S. Slimani, A. Talone, M. Abdolrahimi, P. Imperatori, G. Barucca, D. Fiorani and D. Peddis, *J. Phys. Chem. C*, 2023, **127**, 8840–8849.
29 A.-H. Lu, E. L. Salabas and F. Schüth, *Angew. Chem., Int. Ed.*, 2007, **46**, 1222–1244.
30 E. S. D. T. de Mendonça, A. C. B. de Faria, S. C. L. Dias, F. F. H. Aragón, J. C. Mantilla, J. A. H. Coaquira and J. A. Dias, *Surf. Interfaces*, 2019, **14**, 34–43.
31 J. H. Jang and H. B. Lim, *Microchem. J.*, 2010, **94**, 148–158.
32 L. Maccarino, V. Miglio, G. Paul, G. Golemme, C. Bisio and L. Marchese, *Microporous Mesoporous Mater.*, 2024, **375**, 113178.
33 P. L. Edmiston, L. J. West, A. Chin, N. Mellor and D. Barth, *Ind. Eng. Chem. Res.*, 2016, **55**, 12068–12079.
34 S. Ailawar, A. Hunoor, P. L. Edmiston and U. S. Ozkan, *Ind. Eng. Chem. Res.*, 2025, **64**, 1072–1084.

35 S. Slimani, C. Meneghini, M. Abdolrahimi, A. Talone, J. P. M. Murillo, G. Barucca, N. Yaacoub, P. Imperatori, E. Illés, M. Smari, E. Dhahri and D. Peddis, *Appl. Sci.*, 2021, **11**, 5433.
36 N. C. Roxana, O. Costişor, C. Ianăşi, R. Lazău, L. Săcărescu, D. Nižňanský, A. Ercuța, A.-M. Putz and C. Savii, *Studia UBB Chemia*, 2018, **63**, 15–29.
37 R. Nicola, O. Costişor, M. Ciopec, A. Negrea, R. Lazău, C. Ianăşi, E.-M. Picioruş, A. Len, L. Almásy, E. I. Szerb and A.-M. Putz, *Appl. Sci.*, 2020, **10**, 2726.
38 R. F. Maniur, A. B. Cahaya and A. Manaf, *Fiziya*, 2022, **4**, 78–82.
39 M. Stoia, R. Istratie and C. Păcurariu, *J. Therm. Anal. Calorim.*, 2016, **125**, 1185–1198.
40 M. R. Martina, L. Zoli and E. Sani, *Int. J. Thermofluids*, 2022, **15**, 100169.
41 T. Gu, Y. Zhang, S. A. Khan and T. A. Hatton, *Colloid Interface Sci. Commun.*, 2019, **28**, 1–4.
42 A. K. Ganguli, A. Ganguly and S. Vaidya, *Chem. Soc. Rev.*, 2010, **39**, 474–485.
43 B. Sun, J. Chai, Z. Chai, X. Zhang, X. Cui and J. Lu, *J. Colloid Interface Sci.*, 2018, **526**, 9–17.
44 M. P. Tsyurupa and V. A. Davankov, *React. Funct. Polym.*, 2006, **66**, 768–779.
45 M. Abdolrahimi, M. Vasilakaki, S. Slimani, N. Ntallis, G. Varvaro, S. Laureti, C. Meneghini, K. N. Trohidou, D. Fiorani and D. Peddis, *Nanomaterials*, 2021, **11**, 1787.
46 M. Vasilakaki, N. Ntallis, N. Yaacoub, G. Muscas, D. Peddis and K. N. Trohidou, *Nanoscale*, 2018, **10**, 21244–21253.
47 J. I. Gittleman, B. Abeles and S. Bozowski, *Phys. Rev. B*, 1974, **9**, 3891–3897.
48 J. L. Dormann, D. Fiorani and E. Tronc, in *Advances in Chemical Physics*, Wiley, New York, 1997, vol. XCVIII, pp. 283–494.
49 H. Mamiya, M. Ohnuma, I. Nakatani and T. Furubayashim, *IEEE Trans. Magn.*, 2005, **41**, 3394–3396.
50 C. Cannas, A. Musinu, D. Peddis and G. Piccaluga, *J. Nanopart. Res.*, 2004, **6**, 223–232.
51 S. Pirillo, M. L. Ferreira and E. H. Rueda, *J. Hazard. Mater.*, 2009, **168**, 168–178.
52 G. Celik, S. A. Ailawar, H. Sohn, Y. Tang, F. F. Tao, J. T. Miller, P. L. Edmiston and U. S. Ozkan, *ACS Catal.*, 2018, **8**, 6796–6809.
53 P. L. Edmiston and L. A. Underwood, *Sep. Purif. Technol.*, 2009, **66**, 532–540.
54 E. K. Stebel, K. A. Pike, H. Nguyen, H. A. Hartmann, M. J. Klonowski, M. G. Lawrence, R. M. Collins, C. E. Hefner and P. L. Edmiston, *Environ. Sci.: Water Res. Technol.*, 2019, **5**, 1854–1866.